

The relatively large number of small grains is not unexpected dynamically; it follows clearly from our ejecta scaling law and from our assumption that smaller grains are swept up at roughly the same rate as their more massive brethren. Furthermore, because a substantial population of submicrometer dust is observed in the F and G rings, it might be expected in the E ring. Nevertheless, the excess of small particles in the model's output disagrees with the most straightforward interpretation (1) of all the observations, namely that the E ring has an appreciably lower optical depth in submicrometer particles than in micrometer grains.

This discrepancy may be partially caused by failings of our dynamical simulation [for example, by incorrect size distributions for the ejecta or underestimated loss rates for submicrometer grains (25)]. Nevertheless, we believe that a more likely resolution of this conflict is that submicrometer particles are present, albeit primarily confined to a narrow torus around Enceladus's orbit (Fig. 2). Ground-based measurements of the ring's blue spectrum, which are the strongest constraints to a narrow size distribution, were obtained only for a narrow strip of the E ring. In addition, photometric ratios are based on single images of localized regions. Furthermore, Voyager took only three frames of the E ring's core, near Enceladus' orbit, where our model would suggest small grains should be prevalent; all these images were obtained near a phase angle of 120° and accordingly are not diagnostic of particle size. Under the circumstance where the particle size distribution varies across the ring, as our dynamical model predicts, the photometric modeling technique (1), which assumed a single size distribution for the entire ring, may lead to biased results (26).

Our model shows how dusty rings, such as Saturn's E ring, may be self-generating. High-velocity impacts into satellites sustain the E ring by generating ejecta, whereas ring particles are lost in catastrophic grain-grain collisions. The resulting steady-state ring has a calculable mass and optical depth that agree with the measured quantities. In general, a self-sustaining ring of this type requires only advantageously located source satellites of proper sizes and a mechanism for increasing the relative velocities between particles and satellites, thereby enhancing collisional yields.

REFERENCES AND NOTES

1. M. R. Showalter, J. N. Cuzzi, S. M. Larson, *Icarus* **94**, 451 (1991).
2. M. Horanyi, J. A. Burns, D. P. Hamilton, *ibid.* **97**, 248 (1992).
3. D. P. Hamilton, *ibid.* **101**, 244 (1993).
4. J. E. P. Connerney, L. Davis Jr., D. L. Chenette, in *Saturn*, T. Gehrels and M. S. Matthews, Eds. (Univ. of Arizona Press, Tucson, AZ, 1984), pp. 354–377.
5. J. A. Burns, P. L. Lamy, S. Soter, *Icarus* **40**, 1 (1979).
6. E. J. Öpik, *Interplanetary Encounters: Close-Range Gravitational Interactions* (Elsevier, New York, 1976).
7. W. A. Feibelman, *Nature* **214**, 793 (1967).
8. K. D. Pang, C. C. Voge, J. W. Rhoads, J. M. Ajello, *J. Geophys. Res.* **89**, 9459 (1984).
9. P. K. Haff, A. Eviatar, G. L. Siscoe, *Icarus* **56**, 426 (1983).
10. W. B. McKinnon, *Lunar Planet. Sci.* **14**, 487 (1983).
11. J. D. O'Keefe and T. J. Ahrens, *Science* **198**, 1249 (1977).
12. Spall fragments, which are only lightly shocked because of cancellation of the initial compressional and the reflected rarefaction stress waves, can exceed the projectile in size. See H. J. Melosh, *Impact Cratering: A Geologic Process* (Oxford Univ. Press, Oxford, 1989).
13. W. Frisch, thesis, Lehrstuhl für Raumfahrttechnik der Technische Universität München, München, Germany (1990).
14. W. Frisch, in *Hypervelocity Impacts in Space*, J. A. M. McDonnell, Ed. (University of Kent at Canterbury, Canterbury, UK, 1992), pp. 7–14.
15. D. Koschny, thesis, Lehrstuhl für Raumfahrttechnik der Technische Universität München, München, Germany (1993).
16. A distribution of eccentric orbits having Enceladus' semimajor axis will preferentially strike the leading (trailing) face of exterior (interior) satellites because collisions will occur near apocenter (pericenter). Hence, assuming that impacts cause surface brightening, one can explain why Tethys and Dione, satellites exterior to Enceladus, have brighter leading hemispheres, whereas Mimas, which lies interior to Enceladus, has a brighter trailing hemisphere.
17. B. J. Buratti, *Icarus* **75**, 113 (1988).
18. D. E. Shemansky, P. Matheson, D. T. Hall, H.-Y. Hu, T. M. Tripp, *Nature* **363**, 329 (1993).
19. J. N. Cuzzi and R. H. Durisen, *Icarus* **84**, 467 (1990).
20. D. P. Hamilton and J. A. Burns, *Nature* **365**, 498 (1993); R. E. Johnson *et al.*, *Eos* **74**, 569 (1993).
21. M. R. Showalter and J. N. Cuzzi, *Icarus* **103**, 124 (1993).
22. M. R. Showalter, J. B. Pollack, M. E. Ockert, L. R. Doyle, J. B. Dalton, *ibid.* **100**, 394 (1992).
23. L. Dones, J. N. Cuzzi, M. R. Showalter, *ibid.* **105**, 184 (1993).
24. J. E. Colwell and L. W. Esposito, *ibid.* **86**, 530 (1990).
25. Grains smaller than a few tenths of a micrometer in radius actually gyrate, like electrons and ions, around magnetic field lines. These grains have large velocities relative to circularly orbiting satellites and so they will be swept up more rapidly than we have assumed.
26. The photometric model assumes uniform properties across the ring's expanse, and if that condition is relaxed, the result of a monodisperse size distribution is no longer necessarily valid. Unfortunately, the consequences of relaxing one or another assumption on the derived size distribution are not easily predictable (M. R. Showalter, private communication).
27. J. A. Burns, in *Satellites*, J. A. Burns and M. S. Matthews, Eds. (Univ. of Arizona Press, Tucson, AZ, 1986), pp. 1–38.
28. We thank M. R. Showalter, J. N. Cuzzi, and L. Dones for many useful discussions and acknowledge the assistance of two anonymous reviewers.

17 August 1993; accepted 10 March 1994

Quantum Cascade Laser

Jerome Faist, Federico Capasso,* Deborah L. Sivco, Carlo Sirtori, Albert L. Hutchinson, Alfred Y. Cho

A semiconductor injection laser that differs in a fundamental way from diode lasers has been demonstrated. It is built out of quantum semiconductor structures that were grown by molecular beam epitaxy and designed by band structure engineering. Electrons streaming down a potential staircase sequentially emit photons at the steps. The steps consist of coupled quantum wells in which population inversion between discrete conduction band excited states is achieved by control of tunneling. A strong narrowing of the emission spectrum, above threshold, provides direct evidence of laser action at a wavelength of 4.2 micrometers with peak powers in excess of 8 milliwatts in pulsed operation. In quantum cascade lasers, the wavelength, entirely determined by quantum confinement, can be tailored from the mid-infrared to the submillimeter wave region in the same heterostructure material.

Most solid-state and gas lasers rely on narrow optical transitions connecting discrete energy levels between which population inversion is achieved by optical or electrical pumping (1). In contrast, semiconductor diode lasers (2), including quantum well lasers (3), rely on transitions between energy bands in which conduction electrons and valence band holes, injected into the active layer through a forward-biased *pn* junction, radiatively recombine across the band gap. The band gap essen-

tially determines the emission wavelength (4). In addition, because the population inversion is broadly distributed, in accord with Pauli's principle, between bands having dispersion with opposite curvature, the resulting gain spectrum is relatively broad. These characteristics have profound implications for the operation of semiconductor lasers (3).

We report the design and demonstration, using molecular beam epitaxy (MBE) (5) and band structure engineering (6), of a semiconductor injection laser (quantum cascade laser) that differs in a fundamental way from diode lasers. It relies on only one

AT&T Bell Laboratories, Murray Hill, NJ 07974, USA.

*To whom correspondence should be addressed.

type of carrier (unipolar semiconductor laser) and on electronic transitions between conduction band states arising from size quantization in semiconductor heterostructures. The joint density of states of these transitions and the corresponding gain spectrum are therefore narrow and essentially symmetric.

The quest for such a laser has a 25-year-long history originating with the pioneering proposal by Kazarinov and Suris (7) shortly after the seminal work of Esaki and Tsu (8) on superlattices. However, no experimental realization has so far been reported (9). The potential technological significance of our laser is that the wavelength, being entirely determined by quantum confinement, can be tailored, using the same heterostructure material, over a wide spectral range from the mid-infrared to the submillimeter wave region ($\sim 100 \mu\text{m}$), a portion of the spectrum not easily accessible with diode lasers. In addition, one can use relatively wide band gap, technologically mature materials (such as GaAs- and InP-based heterostructures) without having to rely on temperature-sensitive and difficult-to-process small band gap semiconductors.

Our laser scheme (Fig. 1A) makes use of the discrete electronic states arising from quantum confinement, normal to the layers, in nanometer-thick semiconductor heterostructures grown by MBE (5, 6). Parallel to the layers, these states have plane wave-like energy dispersion. The corresponding energy subbands are nearly parallel because of the small nonparabolicities for wave numbers k_{\parallel} not too far ($\leq 10 \text{ meV}$) from the bottom ($k_{\parallel} = 0$) and for transition energies that are not too large (Fig. 1B) (10). As a result, electrons making radiative transitions to a lower subband (for example, from $n = 3$ to $n = 2$) will all emit photons of essentially the same frequency ν with energy $h\nu = E_3 - E_2$ (Fig. 1B), where h is Planck's constant. The joint density of states of these transitions is therefore similar to a delta function in the absence of broadening (11). If a population inversion is then created between these excited states, the gain spectrum will be correspondingly narrow (collision limited), nearly symmetric, and much less sensitive to thermal broadening of the electron distribution, unlike the gain spectrum associated with interband transitions in semiconductor diode lasers (3).

The laser structure (Fig. 2) was grown by MBE with the $\text{Al}_{0.48}\text{In}_{0.52}\text{As}-\text{Ga}_{0.47}\text{In}_{0.53}\text{As}$ heterojunction material system lattice matched to InP. Electrical pumping was achieved by alternating 25 undoped coupled-well active regions with compositionally graded layers. The graded regions consist of an AlInAs-GaInAs superlattice with constant period, shorter than the electron thermal de

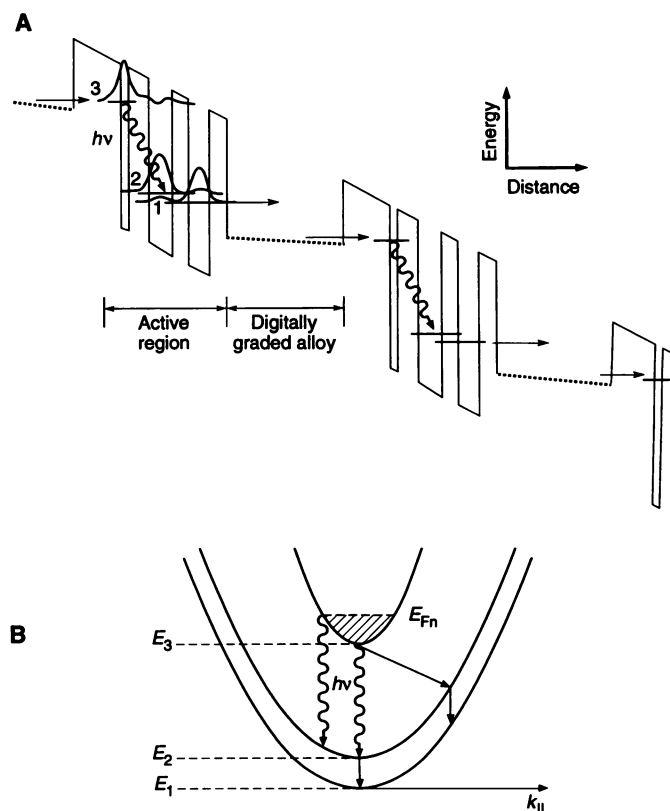
Broglie wavelength, and varying duty cycle to obtain a graded gap pseudoquaternary alloy (12). To minimize space-charge effects caused by injection, the graded regions are n -type doped with silicon. The graded gap varies from lower to higher values in going from left to right in each period of Fig. 1. Thus, at zero applied bias, the band diagram of the structure has an overall sawtooth shape.

If a voltage of the appropriate polarity is applied, the conduction band diagram acquires a staircase shape (Fig. 1A) when the electric field exceeds the opposing quasi-electric field associated with the conduction band grading (13). This occurs in our structure for a field $\sim 10^5 \text{ V/cm}$, corresponding to near flat-band condition in the graded regions (Fig. 1A). Our calculations show that at this bias, the graded regions are quasi-neutral. Electrons relax in the graded regions and are then injected by tunneling into the $n = 3$ excited state (Fig. 1).

The tunneling rate through the trapezoidal barrier is extremely fast, $(\sim 0.2 \text{ ps})^{-1}$, ensuring the efficient filling of level 3. The coupled-well region is essentially a four-level

laser system (1), where a population inversion is achieved between the two excited states $n = 3$ and $n = 2$. The intersubband optical-phonon-limited relaxation time (14), τ_{32} , between these states is estimated to be $\sim 4.3 \text{ ps}$ at $\sim 10^5 \text{ V/cm}$; this process is between states of reduced spatial overlap and accompanied by a large momentum transfer (Fig. 1B) associated with the large intersubband separation; as such, τ_{32} is relatively long. This ensures population inversion between the two states because the lower of the two empties with a relaxation time estimated around 0.6 ps . This efficient relaxation is provided by the adjacent 28 \AA GaInAs well. Strong inelastic relaxation by means of optical phonons with nearly zero momentum transfer occurs between the strongly overlapped and closely spaced $n = 2$ and $n = 1$ subbands (Fig. 1B). Finally, the tunneling escape time out of the $n = 1$ state is extremely short ($\leq 0.5 \text{ ps}$), further facilitating population inversion. This design of the coupled-well region also enhances the injection efficiency into the excited state E_3 by reducing the tunneling escape probability

Fig. 1. (A) Conduction band energy diagram of a portion of the 25-period (active region plus injector) section of the quantum cascade laser. The dashed lines are the effective conduction band edges of the digitally graded electron-injecting regions. Electrons are injected through a 4.5-nm AlInAs barrier into the $n = 3$ energy level of the active region. The latter includes 0.8-nm- and 3.5-nm-thick GaInAs wells separated by a 3.5-nm AlInAs barrier. The reduced spatial overlap between the $n = 3$ and $n = 2$ states and the strong coupling to an adjacent 2.8-nm GaInAs well through a 3.0-nm AlInAs barrier ensure a population inversion between these states. Electrons escape from this well through a 3.0-nm AlInAs barrier. The moduli squared of the relevant wave functions are shown. The calculated energy differences are $E_3 - E_2 = 295 \text{ meV}$ and $E_2 - E_1 = 30 \text{ meV}$. The wavy arrow indicates the laser transition. **(B)** Schematic representation of the dispersion of the $n = 1, 2$, and 3 states parallel to the layers; k_{\parallel} is the corresponding wave number. The bottom of these subbands correspond to energy levels $n = 1, 2$, and 3 indicated in (A). The wavy arrows indicate that all radiative transitions originating from the electron population (shown as shaded) in the $n = 3$ state have essentially the same wavelength. The quasi-Fermi energy E_{Fn} corresponding to the population inversion at threshold ($n_s = 1.7 \times 10^{11} \text{ cm}^{-2}$) is $\sim 8 \text{ meV}$, measured from the bottom of the $n = 3$ subband. The straight arrows represent the intersubband optical-phonon scattering processes; note the fast (subpicosecond) relaxation processes with near-zero momentum transfer between the $n = 1$ and $n = 2$ subbands.



into the continuum. The estimated escape time τ_{esc} is 6 ps, which leads to an injection efficiency $\eta_{\text{in}} = \tau_{\text{esc}}/(\tau_{\text{esc}} + \tau_{32}) \approx 0.6$.

The radiative efficiency of our $3 \rightarrow 2$ laser transition (wavy arrow in Fig. 1A) is estimated to be $\tau_{32}/\tau_R \approx 3 \times 10^{-4}$ at a field $\sim 10^5$ V/cm, where τ_R is the spontaneous emission lifetime, estimated at ~ 13 ns. Calculations show that the product of $|z_{32}|^2 \tau_{32}$ (where $z_{32} = 1.5$ nm is the transition matrix element) is weakly dependent on the electric field. The absence of intentional doping in the active region strongly reduces the linewidth of the $3 \rightarrow 2$ electroluminescence as compared to doped coupled-wells, thus enhancing the peak material gain for the same radiative efficiency (15). Electric field tunable electroluminescence, up to room temperature, has recently been observed by us in similar AlInAs-GaInAs coupled-quantum well heterostructures (16).

Additional layers (waveguide cladding) (Fig. 2) confine to the active region the radiation propagating parallel to the layers. The mode is polarized normal to the layers by the selection rule for intersubband transitions. Calculations of the confinement factor Γ and refractive index n of this single mode waveguide give $\Gamma = 0.46$ and $n = 3.26$, respectively. The samples were lithographically processed into mesa-etched ridge waveguides 12 μm wide. We defined the length of the waveguide (varying from 500 to

720 μm) by cleaving the samples. The cleaved facets provide the mirrors of the laser cavity with a reflectivity $R = 0.27$. Suitable ohmic contacts were provided to the top contact layer and to the substrate. The samples, soldered to a ceramic holder, were mounted in a Helitran flow dewar. Current pulses of 20-ns duration were injected into the device with a 10^{-3} duty cycle, and the emission spectra were obtained with a Nicolet Fourier transform infrared spectrometer with a step-scan and lock-in detection technique.

The spectrum below a 600-mA drive current for a device 500 μm long (Fig. 3) is broad, indicative of spontaneous emission. Above a drive current of 850 mA, corresponding to a threshold current density $J_{\text{th}} = 15$ kA/cm², the signal increases abruptly by orders of magnitude, accompanied by a dramatic line-narrowing. This is direct manifestation of laser action. A plot of optical power versus drive current for a longer laser (720 μm in length) (Fig. 4), obtained by focusing the light with $f/1.5$ optics on a fast, calibrated HgCdTe detector, shows that the threshold is reduced to 11 kA/cm², corresponding to 8 V across the device, with a peak optical power from a single facet of 8.5 mW, limited by the collection efficiency (40%) of the apparatus and by the divergence of the beam ($\pm 40^\circ$) normal to the layers. The laser wavelength does not shift in the current range of Fig. 4, indicating that the electron density in the

excited state $n = 3$ is locked at the threshold value (1, 3). From the threshold current density and the calculated values of τ_{32} and τ_{esc} , we estimate from a simple rate equation argument a population inversion $n_s = 1.7 \times 10^{11}$ cm⁻² comparable to the electron density in the graded region. In a high-resolution spectrum (Fig. 4, inset), well-defined, nearly equally spaced longitudinal modes are observed. The mode spacing $\Delta\nu = 2.175$ cm⁻¹ is in good agreement with the calculated one ($1/2nL = 2.13$ cm⁻¹, where L is the length of the laser). The linewidth of the dominant mode (~ 0.3 cm⁻¹) is presently limited by heating effects and mode hopping during the pulse. For this type of laser, one ultimately expects, in single longitudinal mode continuous wave operation, a Schawlow-Townes type linewidth (17) with negligible linewidth enhancement factor compared with semicon-

Fig. 2. Schematic cross section of the complete $\text{Al}_{0.48}\text{In}_{0.52}\text{As-Ga}_{0.47}\text{In}_{0.53}\text{As}$ laser structure grown by MBE. Indicated are the n -type doping levels and the layer thicknesses in nanometers. The structure has a total of 500 layers. The 18.6-nm-thick digitally graded injectors each comprise six 3.0-nm-thick GaInAs-AlInAs periods; the duty cycle of the AlInAs barrier layers varies from 40 to 77%, top to bottom, to create the pseudoquaternary AlGaInAs variable-gap alloy. The other digitally graded AlGaInAs regions smooth out conduction band barriers between layers (for example, AlInAs and GaInAs). The refractive index discontinuities between the core and cladding regions provide optical confinement for the laser mode. The optical cavity is defined by the Fresnel reflections from two cleaved facets normal to the layers.

Contact layer	GaInAs Sn doped	$n = 2.0 \times 10^{20}\text{cm}^{-3}$	20.0 nm
	GaInAs	1.0×10^{18}	670.0
	AlGaInAs Graded	1.0×10^{18}	30.0
Waveguide cladding	AlInAs	5.0×10^{17}	1500.0
	AlInAs	1.5×10^{17}	1000.0
	AlGaInAs Digitally graded	1.5×10^{17}	18.6
	Active region	undoped	21.1
Waveguide core	GaInAs	1.0×10^{17}	300.0
	AlGaInAs Digitally graded	1.5×10^{17}	14.6
	AlGaInAs Digitally graded	1.5×10^{17}	18.6
	Active region	undoped	21.1
	GaInAs	1.0×10^{17}	300.0
	AlGaInAs Digitally graded	1.5×10^{17}	33.2
Waveguide cladding	AlInAs	1.5×10^{17}	500.0
	Doped n^+ InP substrate		

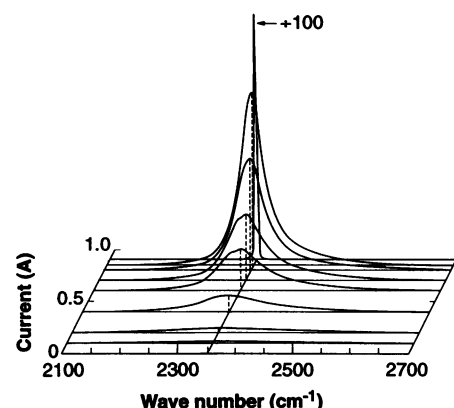


Fig. 3. Emission spectrum of the laser at various drive currents. The strong line narrowing and large increase of the optical power above $I = 850$ mA demonstrates laser action. The spontaneous emission and the laser radiation are polarized normal to the layers. The emission wavelength, $\lambda = 4.26$ μm , is in excellent agreement with the calculated one for the $n = 3$ to $n = 2$ transition (Fig. 1A). The temperature is 10 K.

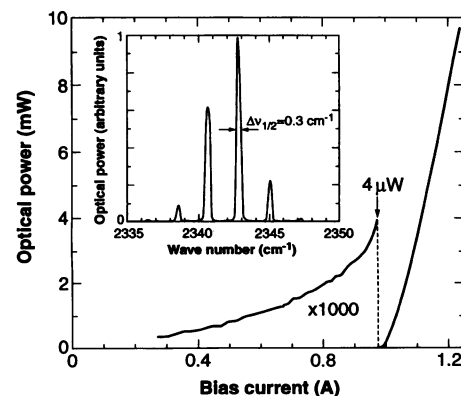


Fig. 4. Optical power versus drive current for a laser at 10 K. (Inset) A high-resolution spectrum with nearly equally spaced longitudinal modes, taken at a current of 1.05 A. We were able to operate this device up to a temperature of ~ 90 K with a threshold current density of ~ 14 kA/cm².

ductor lasers (3, 18) because the refractive index variation induced by the change in carrier number at the peak of the gain curve is essentially zero.

The threshold current density is determined by the condition (1, 3)

$$R \exp(\Gamma G_p - \alpha_i)L = 1 \quad (1)$$

where $G_p = gJ_{th}$ is the peak material gain at threshold and α_i is the internal loss. A good estimate for the normalized gain coefficient g was obtained experimentally from the following independent measurement: The integrated luminescence power was measured at high current density in an identical sample grown on a semi-insulating substrate to minimize losses, but without the cladding regions to eliminate gain effects, and processed in a 45° wedge configuration. The luminescence peak wavelength and linewidth were identical to that of the laser structure. From the measured luminescence power and the well-known Einstein relation between the spontaneous and stimulated emission rates, g was found to be $9 \text{ cm}^{-1} \text{ kA}^{-1} \text{ cm}^{-2}$. We can then recast Eq. 1 in the form

$$J_{th} = \frac{\alpha_M + \alpha_i}{g\Gamma} \quad (2)$$

where α_M is the mirror loss $-\ln(R)/L$ ($= 18.54 \text{ cm}^{-1}$) and the internal loss α_i (estimated to be $\sim 9 \text{ cm}^{-1}$) is a combination of free carrier absorption in the graded regions and in the substrate, lateral waveguide losses, and plasmon losses in the top contact region. From Eq. 2, we obtain $J_{th} = 6.6 \text{ kA/cm}^2$. Considering the relatively large uncertainty in the estimation of the losses, this value is in reasonable agreement with the measured threshold. We were able to operate a few devices at temperatures as high as 88 K with comparable thresholds and clear evidence of spectral narrowing. Improved device processing and heat sinking will allow a systematic study at this and higher temperatures. Preliminary evidence shows that, as expected, the temperature dependence of the threshold current density is much weaker than that in diode lasers (3).

REFERENCES AND NOTES

1. See, for example, A. Yariv, *Quantum Electronics* (Wiley, New York, 1988), chap. 10.
2. R. N. Hall, G. E. Fenner, J. D. Kingsley, T. J. Soltys, R. O. Carlson, *Phys. Rev. Lett.* **9**, 366 (1962); M. I. Nathan, W. P. Dumke, G. Burns, F. H. Dill Jr., G. Lasher, *Appl. Phys. Lett.* **1**, 62 (1962); T. M. Quist *et al.*, *ibid.*, p. 91; N. J. Holonyak and S. F. Bevacqua, *ibid.*, p. 82. The modern double-heterostructure injection laser was demonstrated by H. Kressel and H. Nelson [*RCA Rev.* **30**, 106 (1969)], Zh. Alferov, V. M. Andrei, E. L. Portnoi, and M. K. Trukan [*Sov. Phys. Semicond.* **3**, 1107 (1970)], and I. Hayashi, M. B. Panish, P. W. Foy, and S. Sumski [*Appl. Phys. Lett.* **17**, 109 (1970)]. Its concept was proposed by H. Kroemer [*Proc. IEEE* **51**, 1782 (1963)].
3. For a recent review of semiconductor lasers, see G. P. Agrawal and N. K. Dutta, *Long-Wavelength*

Semiconductor Lasers (Van Nostrand Reinhold, New York, 1986).

4. This holds true also for quantum well lasers, where the band gap of the well material is effectively increased by the quantum confinement of electrons and holes.
5. A. Y. Cho, *J. Cryst. Growth* **111**, 1 (1991).
6. F. Capasso, *Science* **235**, 172 (1987).
7. R. F. Kazarinov and R. A. Suris, *Sov. Phys. Semicond.* **5**, 207 (1971); for a detailed discussion of this and similar schemes, see F. Capasso, K. Mohammed, A. Y. Cho, *IEEE J. Quantum Electron.* **22**, 1853 (1986). For more recent proposals, see A. Kastalsky, V. J. Goldman, J. Abeles, *Appl. Phys. Lett.* **59**, 2636 (1991); J. P. Lohr, J. Singh, R. K. Mains, G. I. Haddad, *ibid.*, p. 2070; S. I. Borenstein and J. Katz, *ibid.* **55**, 654 (1989).
8. L. Esaki and R. Tsu, *IBM J. Res. Dev.* **14**, 61 (1970).
9. Before the invention of the diode laser, a semiconductor laser based on transitions between Landau subbands in a magnetic field was proposed by B. Lax [in *Proceedings of the International Symposium on Quantum Electronics*, C. H. Townes, Ed. (Columbia Univ. Press, New York, 1960), p. 428]. During the last decade, lasers based on infrared emission by hot holes in crossed electric and magnetic fields in *p*-type Ge have been demonstrated. These sources, based on various mechanisms, including cyclotron emission, are of limited technological interest. For a review, see A. A. Andronov, *Sov. Phys. Semicond.* **21**, 701 (1987).
10. The electronic states of our $\text{Al}_{0.48}\text{In}_{0.52}\text{As}-\text{Ga}_{0.47}\text{In}_{0.53}\text{As}$ coupled-well structure (Fig. 1A) were calculated in the envelope function approximation for various electric fields. The material parameters were conduction band discontinuity $\Delta E_c = 0.52 \text{ eV}$, electron effective mass $m_e^*(\text{GaInAs}) = 0.043 m_0$, where m_0 is the free electron mass, and $m_e^*(\text{AlInAs}) = 0.078 m_0$. For the nonparabolicity coefficient, we used $\gamma = 1.13 \times 10^{-18} \text{ m}^2$. Nonparabolicities were taken into account with the method of D. F. Nelson, R. C. Miller and D. A. Kleinman [*Phys. Rev. B* **35**, 7770 (1987)].
11. Narrow ($\sim 1 \text{ meV}$) lifetime-broadened Lorentzian intersubband transitions at energies $\sim 140 \text{ meV}$, with high oscillator strengths, have recently been observed in absorption in high-quality selectively doped $\text{AlGaAs}-\text{GaAs}$ coupled quantum wells. See J. Faist, C. Sirtori, F. Capasso, L. Pfeiffer, K. West, *Appl. Phys. Lett.* **64**, 872 (1994).
12. F. Capasso, H. M. Cox, A. L. Hutchinson, N. A. Olsson, S. G. Hummel, *Appl. Phys. Lett.* **45**, 1193 (1984).
13. F. Capasso, W. T. Tsang, G. F. Williams, *IEEE Trans. Electron Devices* **30**, 381 (1983).
14. P. J. Price, *Ann. Phys.* **133**, 217 (1981).
15. J. Faist *et al.*, unpublished results.
16. J. Faist *et al.*, *Appl. Phys. Lett.* **64**, 1144 (1994).
17. A. L. Schawlow and C. H. Townes, *Phys. Rev.* **112**, 1940 (1958).
18. C. H. Henry, *IEEE J. Quantum Electron.* **19**, 1391 (1983).
19. We thank R. F. Kazarinov, S. Luryi, and D. V. Lang for comments and discussions.

14 February 1994; accepted 28 February 1994

A Mechanism of Lithium Storage in Disordered Carbons

Kenji Sato,* Minoru Noguchi, Atsushi Demachi, Naohiko Oki, Morinobu Endo

High-resolution electron microscopy and lithium-7 nuclear magnetic resonance measurements were carried out for a disordered carbon material, prepared by heat treatment of polyphenylene, in which lithium was stored electrochemically. The nuclear magnetic resonance spectrum suggests the existence of Li_2 covalent molecules in the carbon material. This extra covalent site of lithium storage promises extraordinarily high energy density for secondary batteries.

Graphite can store various kinds of species, such as potassium and bromine, between the crystalline sheets to form stage compounds called graphite intercalation compounds (GICs) (1). Under certain conditions, graphite stores Li ions electrochemically, forming a GIC. The storage process is reversible, so that graphite can be used instead of metallic Li as the negative electrode in Li secondary batteries (2). Various kinds of graphite and carbons have been studied as candidates for the negative electrode material of so-called Li ion batteries (2, 3). The Li ion batteries are expected to lead to weight elimination for portable electronics apparatus such as video cameras and lap-top

personal computers. Advantages include their high electromotive force of around 3 to 4 V; their high energy density, higher than that of any conventional secondary batteries; and their safety, as no metallic Li is used. Recently, some disordered carbons were shown to have a specific capacity much higher than that expected from the first-stage GIC stoichiometry (C_6Li , 372 A·hour/kg) (3, 4), where the Li is inserted at maximum density between each graphite sheet. These extremely high capacities suggest that there may be a mechanism different from the common well-staged compounds of graphite.

We have synthesized a disordered carbon material that stores Li with a mechanism completely different from that in GICs. High-resolution electron microscopy images as well as ^7Li nuclear magnetic resonance (NMR) spectroscopic evidence indicate a Li storage mechanism by an electrochemical process. This phenomenon

K. Sato, M. Noguchi, A. Demachi, N. Oki, Honda Research and Development Co., Ltd., Wako Research Center, 1-4-1 Chuo, Wako-shi, Saitama, 351-01 Japan. M. Endo, Faculty of Engineering, Shinshu University, 500 Wakasato, Nagano, 380 Japan.

*To whom correspondence should be addressed.